To appear in Proceedings of VMV 2013

Vision, Modeling, and Visualization (2013)
Michael Bronstein, Jean Favre, and Kai Hormann (Eds.)

Local Extraction of Bifurcation Lines

Gustavo M. Machado, Filip Sadlo, and Thomas Ertl

Visualization Research Center, University of Stuttgart, Germany

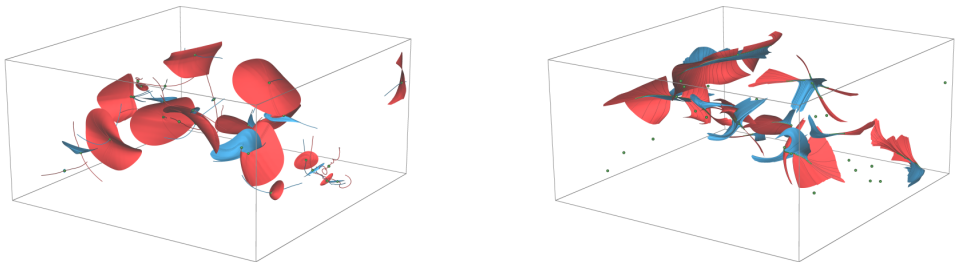

(a) (b)

Figure 1: *Buoyant Flow data set. (a) Traditional visualization by means of 1D/2D manifolds (red, blue) of (spiral) saddle critical points (green). (b) Our visualization by means of 2D manifolds (red, blue) of bifurcation lines (green curves) provides insight in cases where only one or no critical point at all is involved. Note that in (a) there are also 2D manifolds not related to bifurcation lines (e.g., those of spiral saddles at bottom right), but since those manifolds that are present in both (a) and (b) are consistent, the union of both provides the full topological structure.*

Abstract

We present local extraction of bifurcation lines together with extraction of their manifolds, a topological feature that has not yet been sufficiently recognized in scientific visualization. The bifurcation lines are extracted by a modification of the vortex core line extraction techniques due to Sujudi-Haimes, and Roth-Peikert, both formulated using the parallel vectors operator. While the former provides acceptable results only in configurations with high hyperbolicity and low curvature of the bifurcation lines, the latter operates only well in configurations with low hyperbolicity but is able to perform well with strong curvature of the bifurcation lines, however, with the drawback that it often fails to provide a solution. We present refinement of the solutions of the parallel vectors operator as a means to improve both criteria and, in particular, to refine the solutions of the Sujudi-Haimes criterion in cases where the Roth-Peikert criterion fails. We exemplify our technique on synthetic data, data from computational fluid dynamics, and on magnetohydrodynamics data. As a particularly interesting application, we demonstrate that our technique is able to extract saddle-type periodic orbits locally, and in case of high hyperbolicity at higher accuracy than traditional techniques based on integral curves.

Categories and Subject Descriptors (according to ACM CCS): I.6.6 [Simulation and Modeling]: Simulation Output Analysis—; J.2 [Physical Sciences and Engineering]: Physics—

1. Introduction

Bifurcation lines, as proposed by Perry and Chong [PC87], represent streamlines that exhibit one converging and one diverging 2D manifold of streamlines (Fig. 2) and, surprisingly, have not yet been sufficiently recognized in scientific visualization. In his thesis [Rot00], Roth states that bifurcation lines can be obtained by extending Kenwright's local criterion [KHL99], which was defined for attachment and separation lines in 2D vector fields on surfaces, to 3D vector fields. Roth also mentions that the resulting 3D criterion is identical to the vortex core line criterion by Sujudi and Haimes [SH95], with the only difference that instead of requiring complex eigenvalues of the velocity gradient, real eigenvalues are required. Finally, he also notes that this technique would work only for sufficiently straight bifurcation lines, for the same reasons that motivated his higher-order extraction of vortex core lines [RP98]. As stated in that paper, however, this technique for vortex core lines can provide better results in some cases but may still fail in others.

In this paper we modify and examine both vortex core line extraction techniques, that of Sujudi and Haimes [SH95], and that by Roth and Peikert [RP98], for the extraction of bifurcation lines. Beyond that, we introduce refinement of the resulting curves toward the aimed bifurcation lines, mak-

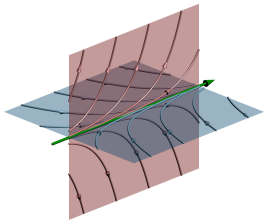

Figure 2: *Bifurcation line (green, according to [PC87]), with two 2D manifolds of streamlines, one converging to the bifurcation line in forward, and one in reverse time.*

ing use of the parallel vectors operator due to Peikert and Roth [PR99], and present a technique to extract the 2D manifolds of bifurcation lines. One of our results is that in our experiments, as expected, modified [RP98] provided better results (required less refinement) than modified [SH95], but there were many cases where modified [RP98] failed to generate a result at all. In many of these cases modified [SH95] still generated an inaccurate result, and applying our refinement provided accurate results in these cases.

Bifurcation lines are closely related to the concept of saddle connectors introduced by Theisel et al. [TWHS03], which represent intersection curves of the 2D manifolds of two saddle-type critical points (Fig. 3(a)). Critical points are isolated zeros of a vector field and those of type saddle can be identified by hyperbolic field behavior, i.e., the eigenvalues of the velocity gradient exhibit both positive and negative real parts. Manifolds that consist of streamlines converging to the saddle in positive time are called stable while those that converge in reverse time are called unstable. We refer the reader to Asimov's notes on topology [Asi93] for a thorough introduction to vector field topology. Since 1D and 2D manifolds consist of streamlines, their intersection is again a streamline. Saddle connectors represent bifurcation lines close to the respective critical points (Fig. 3(b)) since there they are part of the hyperbolic dynamics of the saddle point. In other words, the 1D manifold of saddle-type critical points is always part of the respective 2D manifold of a bifurcation line (Fig. 3(b)).

A final observation is that saddle-type periodic orbits (Fig. 5) resemble closed saddle connectors, however, without a critical point along them. For this reason, saddle periodic orbits cannot be obtained by intersecting 2D manifolds of saddle-type critical points. Nevertheless, in analogy to saddle connectors, at least a part of a saddle-type periodic orbit has to represent a bifurcation line, too (Fig. 5). While one might think that obtaining only parts of saddle connectors and saddle-type periodic orbits represents a limitation, rather the opposite is the case. Bifurcation lines provide insight into the hyperbolic dynamics of a vector field with respect to its topological structure, similar to saddles. Beyond that, bifurcation lines can be present in absence of critical points, saddle connectors, or saddle-type periodic orbits, complementing traditional vector field topology (Figs. 1 and 3).

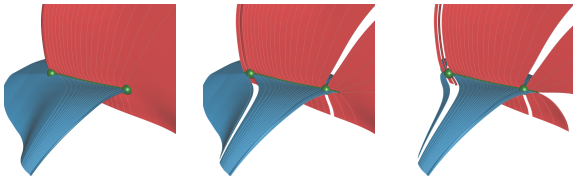

(a) (b) (c)

Figure 3: *Solar MHD data set. (a) Saddle connector (green) represents intersection curve between stable 2D manifold (blue) of left critical point (green) and unstable 2D manifold (red) of right critical point. 2D manifolds are limited by the respective 1D manifolds (dark red and dark blue lines) of the other saddle-type critical point. (b) Same view but with manifolds of bifurcation line (green). 1D manifolds of critical points are consistent with 2D manifolds of bifurcation line. Bifurcation line and thus also its 2D manifolds exhibits gaps at the critical points. (c) Same as (b) but without seed curve connection (Fig. 7(e)) would lead to unnecessary gaps.*

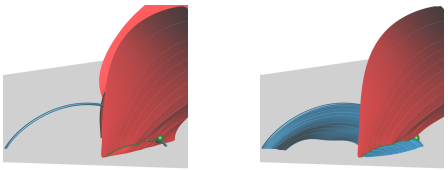

(a) (b)

Figure 4: *Solar MHD data set. (a) Traditional visualization. Saddle-type critical point (green point) is close to domain boundary (gray). The second saddle-type critical point that would be needed for obtaining the saddle connector is not available (located outside the domain). Hence, the 1D manifold (blue) and the 2D manifold (red) of the saddle provide only limited insight. (b) 2D manifolds (red and blue) of the bifurcation line (green line in (a) and (b), touching boundary at the bottom of the image) provide full topological insight.*

All in all, in vector fields defined on unbounded domains, parts of bifurcation lines could be determined by marking each point of saddle connectors and periodic orbits that exhibits hyperbolic behavior. Although this approach would require the costly extraction of periodic orbits and integration of streamlines, it could work for such vector fields. However, it has to be noted that accurate numerical integration of streamlines in hyperbolic regions, i.e., along bifurcation lines (or hyperbolic trajectories [Hal00]), is often a very difficult undertaking because in either, forward or reverse, direction of integration the curve is repelled from the bifurcation line as integration errors are growing exponentially. The white streamline in Fig. 5(a) exemplifies this problem with a saddle-type periodic orbit with medium hyperbolicity. In contrast, our locally extracted bifurcation line captures the entire orbit. It has to be noted, however, that saddle orbits with very low hyperbolicity can be integrated and are also amenable to identification with Poincaré maps (Fig. 5(d)).

The situation is, however, different in vector fields on bounded domains. There, one or both saddle points that are

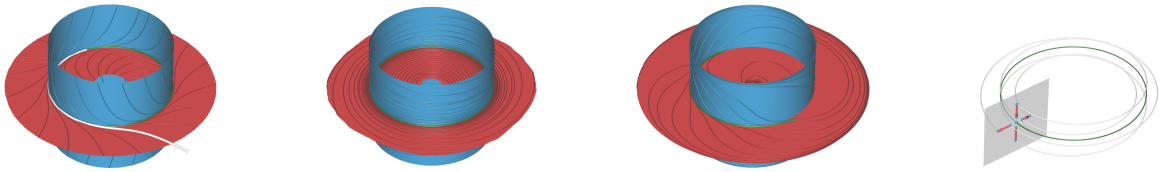

(a) (b) (c) (d)

Figure 5: *Saddle Orbit data sets. (a) Slow orbit (I) (rotation 0.4) (cf. Fig. 6(a)). Periodic orbit is captured as a bifurcation line with refined* $\mathbf{v}\|\mathbf{a}$ *(green), providing stable (blue) and unstable (red) manifolds. Due to the substantial hyperbolicity, we did not succeed in obtaining the periodic orbit by integration of a streamline (white curve). (b) Fast orbit (IV) (rotation 10.0). Periodic orbit is captured as a bifurcation line with refined* $\mathbf{v}\|\mathbf{b}$ *(green). (c) Orbit (VI) that exhibits high hyperbolicity at left but zero hyperbolicity at right. Only the sufficiently hyperbolic (left) part of the bifurcation line is obtained with refined* $\mathbf{v}\|\mathbf{a}$ *(*$\mathbf{v}\|\mathbf{b}$ *failed). Note, however, that the right end of the bifurcation line deviates, i.e., the refinement aligned it with a streamline different to the bifurcation line. Nevertheless, this has negligible impact, since the 2D manifolds are obtained using "connected" seeding curves (Fig. 7(e)), resulting in complete 2D manifolds. (d) Analysis of the periodic orbit (b) with a Poincaré map (gray).*

necessary to extract a saddle connector, or part of a periodic orbit, may be located outside the domain. In these cases, it would be impossible to obtain the respective topological constructs based on streamline integration (Fig. 4(a)). Boundary switch connectors [WTHS04] are an alternative to saddle connectors in bounded domains but they depend on the domain boundary. Local extraction, in contrast, does not make a difference if part of a bifurcation line, saddle connector, or periodic orbit is located outside the domain (Fig. 4(b)).

2. Related Work

The works related most closely to this paper are the saddle connectors due to Theisel et al. [TWHS03] and the concept of saddle-type periodic orbits.

Similar to critical points, periodic orbits also represent objects that are invariant under the action of the flow. Periodic orbits represent isolated closed streamlines, i.e., closed streamlines with no neighboring closed streamline. Similar to critical points, periodic orbits can be classified into different types. This can be achieved by means of the Poincaré map, a map that captures the neighborhood of the periodic orbit with respect to a "full revolution" (Fig. 5(d)). The Poincaré map is obtained by placing a planar disc such that the periodic orbit intersects it at a single point $\mathbf{p}$. By seeding other streamlines in the vicinity of $\mathbf{p}$ and detecting the point where they intersect the disc after one revolution, a 2D map is obtained (arrows in Fig. 5(d)). The eigenvalues of the Jacobian of this map at $\mathbf{p}$ define the type of the periodic orbit. If both eigenvalues are positive and one of them smaller than one while the other is larger than one, the orbit is of type saddle (e.g., Figs. 5 and 9). If both eigenvalues are negative, the orbit is of type twisted saddle (Fig. 9(b)). Both orbits give rise to two 2D manifolds: one manifold converging to the orbit in forward and one in reverse time. In case of twisted saddle orbits, the 2D manifolds represent Möbius strips. Similar to critical points, there are also source and sink types of periodic orbits but these do not give rise to manifolds. A recent technique [KRRS13] extracts saddle-type periodic orbits based on the finite-time Lyapunov exponent.

Closely related to vector field topology but usually not considered topological constructs are vortex core lines. These lines represent the "axis" of vortices and they provide a concise representation of vortical flow. Various approaches have been presented so far for their extraction. Sujudi and Haimes [SH95] extract them as those loci where velocity is parallel to the real eigenvector of the velocity gradient with the additional requirement that the other two eigenvectors are complex. In Roth's formulation [Rot00] of the helicity-based visualization approaches by Levy et al. [LDS90], vortex core lines are defined as those locations where vorticity, i.e., the curl of velocity, is parallel to velocity. Weinkauf et al. [WSTH07] and Fuchs et al. [FPH*08] extend [SH95] for time-dependent flow. Peikert and Roth [PR99] identified the framework of line-type feature extraction as the loci where two vector fields are parallel. Roth and Peikert [RP98] extended the approach [SH95] to higher order. They identified that the approach [SH95] represents the locations where streamlines are straight, reformulated it as the points where acceleration is parallel to velocity, and based on this they extended the approach to a higher order by formulating a criterion that extracts those points of streamlines that exhibit zero torsion. Sahner et al. [SWH05] define vortex core lines as valley lines of λ_2, a scalar field introduced by Jeong and Hussain [JH95] indicating vortex regions, where negative.

In this paper we make use of modified versions of the approaches [SH95] and [RP98] for extracting bifurcation lines. In this respect, the union of the respective vortex core lines, bifurcation lines, and constructs from traditional vector field topology represents an extended topological representation.

3. Extraction of Bifurcation Lines

3.1. Parallel Vectors Operator

Many line-type features can be formulated as the set of loci where two (derived) vector fields are parallel (note that throughout this paper we use the term parallel, denoted as $\|$, also for the antiparallel configuration). In their framework, called the parallel vectors operator, Peikert and Roth [PR99]

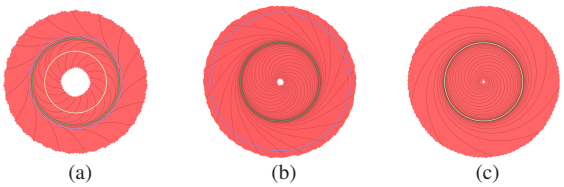

(a) (b) (c)

Figure 6: *Saddle Orbit data sets. View on the planar 2D manifold. (a) Slow orbit (I) (rotation 0.4) (cf. Fig. 5(a)). Solution of* $\mathbf{v}\|\mathbf{a}$ *(purple) is close to refined* $\mathbf{v}\|\mathbf{a}$ *(green), while* $\mathbf{v}\|\mathbf{b}$ *(yellow) deviates substantially due to strong hyperbolicity. (b) Faster orbit (II) (rotation 1.3) (cf. Fig. 7(b)). Solution of* $\mathbf{v}\|\mathbf{a}$ *(purple) deviates substantially but* $\mathbf{v}\|\mathbf{b}$ *provides no solution at all, while refined* $\mathbf{v}\|\mathbf{a}$ *(green) obtains correct solution (cf. Fig. 7(b)). (c) Fast orbit (III) (rotation 3).* $\mathbf{v}\|\mathbf{a}$ *fails while* $\mathbf{v}\|\mathbf{b}$ *(yellow) is very close to refined* $\mathbf{v}\|\mathbf{b}$ *(green).*

formulate different line-type features by means of this approach and provide an algorithm for their efficient extraction. The framework consists of two vector fields $\mathbf{v}$ and $\mathbf{w}$ and solves for the set of points where $\mathbf{v}\|\mathbf{w}$, formulated as

$$\mathbf{v} \times \mathbf{w} = \mathbf{0} \,. \tag{1}$$

In our implementation, we use the "analytic solution for triangulated faces" approach from [PR99], i.e., we triangulate non-triangular faces and solve for the solutions of Eq. 1 thereon, as this approach is faster and typically provides the same results as their approach based on Newton iterations.

Once these "raw" features are obtained, one typically needs to suppress false positives (noise). We follow the approach from [PR99] and reject those parts of features where the angle $\alpha(\boldsymbol{\vartheta}, \mathbf{v}) := cos^{-1}(|\boldsymbol{\vartheta} \cdot \mathbf{v}|/(\|\boldsymbol{\vartheta}\| \cdot \|\mathbf{v}\|))$, defined as the angle between the vector field $\mathbf{v}$ and the tangent $\boldsymbol{\vartheta}$ of the feature line, exceeds the user-defined threshold $\tau_\alpha \geq 0$. The rationale behind this is that many line-type features, including bifurcation lines, conceptually represent streamlines of $\mathbf{v}$ or $\mathbf{w}$. Note that in typical data sets τ_α has to be chosen comparably large, because the criteria often have problems in detecting the exact location of the feature. As a second filtering approach, which is applied subsequently, we require a minimum length τ_μ of the features according to [PS08], to suppress short lines that represent erroneous or weak features. The result of the procedure is a set of (closed) polylines.

3.2. Modification of Vortex Core Line Criteria

As described in Sec. 2, the criterion [SH95] identifies a vortex core line in 3D flow where velocity $\mathbf{v}$ is parallel to the real eigenvector of $\nabla\mathbf{v}$, or in other words, $\mathbf{v}$ is parallel to the steady formulation of acceleration $\mathbf{a} := (\nabla\mathbf{v})\mathbf{v}$, resulting in

$$\mathbf{v} \,\|\, \mathbf{a} \,, \tag{2}$$

with the additional requirement that the other two eigenvectors (and hence also the other two eigenvalues) are complex.

Roth states in his thesis [Rot00] that if one instead requires all eigenvalues to be real, the resulting curves would include bifurcation lines, assuming that the bifurcation lines are sufficiently straight. Since Eq. 2 in this case holds if *any* of the three eigenvectors of $\nabla\mathbf{v}$ is parallel to $\mathbf{v}$, one needs to test for bifurcation line behavior. As illustrated in Fig. 2, a bifurcation line is characterized by hyperbolic behavior in sections perpendicular to the line, i.e., there must be one direction that converges toward the line in forward and one in reverse time if the vector field is projected to that plane. Such a hyperbolic behavior can be characterized in 2D flow by $\det(\nabla\mathbf{v}) < 0$. Hence, besides rejecting feature points where $\alpha(\boldsymbol{\vartheta}, \mathbf{v})$ exceeds τ_α, we additionally require a minimum feature strength $\tau_\chi > 0$, i.e., we project $\nabla\mathbf{v}$ onto the plane perpendicular to $\mathbf{v}$, compute its determinant d and reject the feature point if $d/\|\mathbf{v}\| > -\tau_\chi$. Finally, we reject those lines shorter than τ_μ. Please note that we denote this technique for bifurcation line extraction also as $\mathbf{v}\|\mathbf{a}$ or simply Eq. 2. An example result is shown in Fig. 6(a) (purple).

The higher-order criterion for vortex core lines due to Roth and Peikert [RP98] identifies vortex core lines as those loci where velocity $\mathbf{v}$ is parallel to the steady formulation of the jerk vector $\mathbf{b} := (\nabla\mathbf{a})\mathbf{v} = (\nabla((\nabla\mathbf{v})\mathbf{v}))\mathbf{v}$, resulting in

$$\mathbf{v} \,\|\, \mathbf{b} \,, \tag{3}$$

with the additional requirement that $\nabla\mathbf{v}$ exhibits one real and two complex eigenvalues. While Eq. 2 identifies points with zero streamline curvature as belonging to a vortex core line, Eq. 3 extends the requirement to zero streamline torsion, i.e., locally planar streamlines. The motivation for this definition is that the solutions of Eq. 2 are displaced from the aimed vortex core line the more this core line is curved and the slower the flow rotates around the core line compared to the velocity along the core line. In other words, Eq. 2 fails for bent vortices, in particular if they exhibit a large longitudinal speed. Interestingly, this is also the case for the derived bifurcation line criterion Eq. 2, as demonstrated in Fig. 6. The reason for this is that it identifies the points of zero streamline curvature (see also blue curve in Fig. 7(c)). It is apparent in Fig. 6 that Eq. 3 performs substantially better, however, at the drawback that it may fail at providing a solution.

We modify the approach of Roth and Peikert [RP98] accordingly for bifurcation lines, i.e., as in the case of the criterion by Sujudi and Haimes [SH95], we require that all eigenvalues are real. Besides the difference in the parallel vectors definition, i.e., Eq. 3 instead of Eq. 2, the procedure is identical. We denote this modified technique as $\mathbf{v}\|\mathbf{b}$ or simply Eq. 3. An example result is provided in Fig. 6(a) (yellow).

3.3. Refinement of Parallel Vectors Solutions

As demonstrated in Fig. 6, $\mathbf{v}\|\mathbf{b}$ is often more accurate than $\mathbf{v}\|\mathbf{a}$: it provides very accurate results for high velocities (relative to hyperbolicity) along the bifurcation line. However, there are many cases where it fails to provide a result (e.g., Figs. 1, 6(b), 8, 9, and 10). Some of these cases are amenable to extraction by $\mathbf{v}\|\mathbf{a}$, however with the drawback that $\mathbf{v}\|\mathbf{a}$

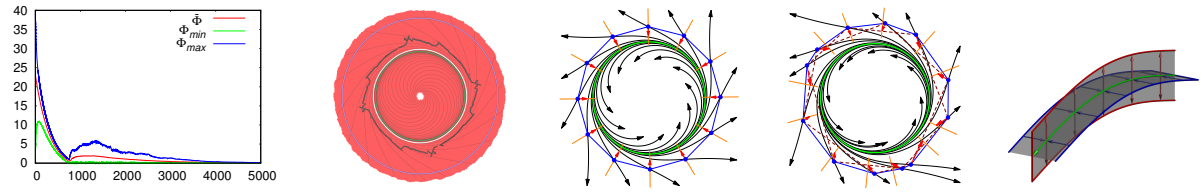

(a) (b) (c) (d) (e)

Figure 7: *(a) Convergence plots of refinement. (b) Impact of regularization (data set II): without regularization (black) and with (green). (c) Refinement illustrated at the example of the radial manifold from Fig. 5(a): bifurcation line (saddle orbit) (green), solution of zero streamline curvature* $\mathbf{v}\|\mathbf{a}$ *(blue), planes normal to tangent of blue curve (orange), and correction vector (red). Small steps along the correction vectors are applied iteratively, making the blue curve converge toward the bifurcation line. (d) Same as (c) illustrating impact of regularization in cases of uneven distribution of vertices of blue polyline. (e) Seed curve generation for 2D manifolds of bifurcation lines. Two seed curves are generated by offsetting from the bifurcation line (green) along the major eigenvector (red) at each point of the line, and two curves by offsetting in the opposite direction of the minor eigenvector (blue). The red curves are connected at the outflow end of the bifurcation line (at the green arrow head), while the blue curves are connected at the inflow end, resulting in two seeding curves.*

does not provide sufficient accuracy for practical applications such as manifold extraction (Fig. 8). To this end we present refinement of parallel vectors solutions. In particular, we refine solutions of $\mathbf{v}\|\mathbf{a}$ in cases where $\mathbf{v}\|\mathbf{b}$ fails.

Figure 7(c) illustrates a typical solution of $\mathbf{v}\|\mathbf{a}$ (in blue) when applied for the extraction of curved bifurcation lines (green). Although it solved $\mathbf{v}\|\mathbf{a}$, it did not provide a solution that is close to a streamline, i.e., $\alpha(\boldsymbol{\vartheta},\mathbf{v})$ is comparably large. Quite large τ_α are necessary to obtain a solution at all in such cases. The necessity of using large τ_α indicates that the result is of low quality, i.e., substantially displaced from the aimed bifurcation line. In contrast, Figs. 6(b) and 6(c) illustrate for the example of refined $\mathbf{v}\|\mathbf{a}$ and $\mathbf{v}\|\mathbf{b}$ that the bifurcation line is well captured if $\alpha(\boldsymbol{\vartheta},\mathbf{v})$ is negligible.

Hence, our motivation is to refine solutions of $(\mathbf{v}\|\mathbf{a})$ in order to reduce $\alpha(\boldsymbol{\vartheta},\mathbf{v})$, i.e., we want to apply the least necessary deformation to make them fit a streamline as close as possible. The recent approach by Martinez et al. [MSRT13] to obtain streamsurfaces by deforming arbitrary surfaces to be as tangential as possible to a vector field would be a possible way to go. In this paper, however, we follow a much simpler approach, also because application of [MSRT13] would exceed the scope of this paper. Nevertheless, we think that it would be worthwhile to investigate it as future work.

We employ a gradient descent approach. At each iteration, we estimate the tangent $\boldsymbol{\vartheta}_i$ of the feature polyline at each of its vertices $\mathbf{c}_i$ by $\boldsymbol{\vartheta}_i := \mathbf{c}_{i+1} - \mathbf{c}_{i-1}$ (clamping at the boundaries of open feature lines) and construct a plane normal to that tangent (orange in Figs. 7(c) and (d)). Inside this plane we employ a step in the direction that reduces $\alpha(\boldsymbol{\vartheta}_i,\mathbf{v}_i)$, i.e., along $-\nabla\alpha(\boldsymbol{\vartheta}_i,\mathbf{v}_i)$ (red in Figs. 7(c) and (d)), with $\mathbf{v}_i$ representing the velocity at $\mathbf{c}_i$. We estimate $\nabla\alpha(\boldsymbol{\vartheta}_i,\mathbf{v}_i)$ by central differencing of $\alpha(\boldsymbol{\vartheta}_i,\mathbf{v}_i)$ using a four-neighbor stencil in the plane. Because Newton iterations would choose a different step size for each vertex in generic setups and would perturb the tangents, we use the same step size Δt for all vertices and reduce Δt after each iteration: $\Delta t_{new} = \delta\Delta t_{old}$, in our experiments we used $\delta = 0.999$ and set Δt initially to 0.01 times the cell size. Centering the orange refinement planes at the respective vertex, as Fig. 7(c) might suggest, would, however, lead to uneven distribution of the vertices along the polyline in asymmetric configurations, i.e., the polyline segments would tend to vary in size. This would affect the estimation of the tangent and hence make the refinement unstable (Fig. 7(b) (black)). To avoid this, we employ regularization, i.e., we translate the planes along $\boldsymbol{\vartheta}_i$ such that they intersect $\boldsymbol{\vartheta}_i$ at $(\mathbf{c}_{i+1}+\mathbf{c}_{i-1})/2$, as illustrated in Fig. 7(d). This leads to a more uniform distribution of the polyline vertices during refinement and hence better convergence (Fig. 7(b)).

The effect of our refinement is also illustrated in Fig. 6. For evaluation/monitoring of the refinement, we compute the absolute flux of $\mathbf{v}$ across the segments of the polyline. We discretize each segment $\mathbf{s}_i := \mathbf{c}_{i+1} - \mathbf{c}_i$ into n parts of equal length, interpolate $\mathbf{v}$ at the center of each part resulting in $\mathbf{v}_j$, and compute the absolute flux ϕ_i across segment i as:

$$\phi_i := \frac{\|\mathbf{s}_i\|}{n} \sum_{j=1}^{n} \left\| \mathbf{v}_j - \frac{\mathbf{v}_j \cdot \mathbf{s}_i}{\|\mathbf{s}_i\|^2} \cdot \mathbf{s}_i \right\| . \tag{4}$$

We monitor its minimum $\phi_{\min}$, maximum $\phi_{\max}$, and average $\overline{\phi}$ over all polyline segments, and plot them (Fig. 7(a)). There, the fluxes dropped fast until a local minimum at iteration 744 (white curve in Fig. 7(b)) and then slowly to the green curve in 4000 iterations, which took 2.409 seconds (Table 1).

4. Extraction of Bifurcation Manifolds

As introduced in Sec. 1, each bifurcation line gives rise to a 2D manifold that converges to it in forward time and to a 2D manifold that converges in reverse time (Fig. 2). Since a bifurcation line typically represents a streamline, starting a streamsurface from this line would degenerate to a streamline itself. Similar to the extraction of 2D manifolds of saddles, one needs to seed the streamsurface at some offset from the bifurcation line. In the case of saddle points, it is common practice to use a closed curve for seeding and to offset

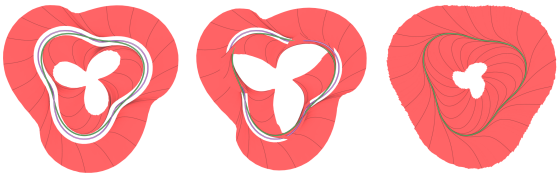

(a) (b) (c)

Figure 8: *Evaluation of bifurcation lines by smallest possible seeding offset during manifold generation. More accurate (more streamline-like) bifurcation lines allow for smaller seeding offset. The underlying data set (V) exhibits additional oscillation of the periodic orbit, causing* $\mathbf{v}\|\mathbf{b}$ *to fail. (a) Manifold (red) computed from solution of* $\mathbf{v}\|\mathbf{a}$ *(purple) with manually found minimum offset of 1.5 that still assures that manifolds extend to correct side of bifurcation line (in contrast to (b) where offset was set to 1.0). (c) Same as (a) but manifold computed from refined* $\mathbf{v}\|\mathbf{a}$ *(green) allows for much smaller offset (smaller than 0.05).*

this curve from the critical point along the eigenvectors of $\nabla\mathbf{v}$. In analogy, we generate a seeding curve for each of the two 2D manifolds at a small offset from the bifurcation line (Fig. 7(e)). The seeding curves for the manifolds that converge to the bifurcation line in forward time are offset in opposite direction to the minor eigenvector and integrated in reverse time, while those converging to it in reverse time are offset along the major eigenvector and integrated forward.

Interestingly, this straightforward approach is not optimal: it would result in unnecessary gaps, as shown in Fig. 3(c). These gaps are avoided if the forward seeding curves are connected at the outflow end of the bifurcation line and the reverse ones are connected at its inflow end (Fig. 7(e)), resulting in manifolds that are more consistent with the 2D manifolds of saddle-type critical points (Fig. 3(b)). As a consequence, this seeding approach is able to extract periodic orbits by intersecting the two manifolds even in cases where the bifurcation line captures only part of the orbit (Fig. 5(c)).

As in the case of the extraction of 2D manifolds of saddle points, where the allowable offset depends on the accuracy of the critical point extraction, the size of the offset is limited by the accuracy of the bifurcation line extraction, too. If the offset is chosen too small, at least parts of the manifolds are advected to the wrong side of the bifurcation line. Hence, the required offset is an expressive measure for the accuracy of an extracted bifurcation line. It can be determined only for the reason of quality assurance, or it is obtained as a byproduct during manifold extraction. Fig. 8 illustrates this in the context of the evaluation of $\mathbf{v}\|\mathbf{a}$ and refined $\mathbf{v}\|\mathbf{a}$.

5. Results

We evaluate our approach using different vector field data. As (incompressible) liquid flow fields at moderate Reynolds numbers exhibit negligible divergence and magnetic fields are divergence-free, critical points as well as periodic orbits of type (spiral) source and sink do not need to be considered in these data. Hence, the remaining stable traditional topological constructs in such 3D vector fields are saddle-type critical points (and the resulting saddle connectors), and (twisted) saddle periodic orbits. As detailed in Sec. 1, both of these constructs contain bifurcation lines. We investigate our technique in the field of computational fluid dynamics (CFD) in Sec. 5.2, as it is a common source of vector fields, and magnetohydrodynamics (MHD) data of the solar corona in Sec. 5.3. But since we did not succeed in finding a CFD or MHD data set that contains a saddle-type periodic orbit, we developed respective analytic models, covered in Sec. 5.1. Note that we highlight some of the streamlines of the 2D manifolds to depict flow direction.

Table 1: *Performance measurements. Total includes extraction (Sec. 3.2), refinement (Sec. 3.3), and filtering (Sec. 3.2).*

Data	Time[s]		
	Refine	Filter	Total
Buoyant Flow (Fig. 1(b))	3.393	0.196	9.145
Saddle Orbit I (Figs. 5(a) and 6(a) (green))	0.662	0.371	1.597
Saddle Orbit II (Figs. 6(b) and 7(b) (green))	2.409	0.373	3.343
Saddle Orbit III (Fig. 6(c) (green))	1.076	0.365	2.367
Saddle Orbit IV (Fig. 5(b))	0.006	0.367	1.320
Saddle Orbit V (Figs. 8 (green))	0.436	0.366	1.361
Saddle Orbit VI (Fig. 5(c))	0.631	0.367	1.514
Saddle Orbit VII (Fig. 9 (green))	0.458	0.368	2.989
Solar MHD (Fig. 10(b))	43.848	14.964	81.303

Table 1 provides the timings of our approach for the data sets used in our results. Our experiments were performed on a Linux-based system consisting of an Intel(R) Core(TM) i7-2600 CPU at 3.4GHz with 8GB of RAM and equipped with a NVidia GeForce GTX 560 Ti with 2GB of memory. Note that our prototype was not optimized for performance and we believe that there is potential for further acceleration.

5.1. Synthetic Periodic Orbits

For investigating our technique in the context of periodic orbits, we developed two similar mathematical models of saddle-type periodic orbits and sampled both on a Cartesian grid of 60^3 nodes and extent of 59^3.

The first model represents an open vector field (with flux across its domain boundaries) and exhibits a saddle-type periodic orbit while the hyperbolic influence is not spatially bounded, i.e., it extends throughout the domain. Besides the definition of the radius of the orbit, it provides parameters for the radial and axial linear growth of the respective vector components with respect to the distance from the orbit, i.e., the hyperbolicity, a parameter for the speed of the superimposed rotation along the orbit, amplitude and frequency to add a radial sine oscillation of the orbit, and amplitude and frequency to add an axial sine oscillation of the orbit.

The second model represents a spatially bounded 2D hyperbolic region, oriented perpendicular to the orbit, bounded with a cosine profile and moving along the orbit. It provides parameters, additional to the first model, to set the speed of twist (i.e., rotation around the orbit) of the hyperbolic region

as it moves along the orbit, parameters to define the size of the hyperbolic region, and to vary the hyperbolic strength of the region while it moves along the orbit.

The first model gave rise to the following data sets. The data set I, visualized in Figs. 5(a) and 6(a), exhibits low rotation (0.4) along the orbit. The data set II from Figs. 6(b) and 7(b) differs from that only in terms of rotation along the orbit, which is 1.3 in this case. In the data set III from Fig. 6(c), the rotation is 3, and the data set IV of Fig. 5(b) differs once more only in terms of the rotation along the orbit, which is 10.0 there. One exception is the data set V from Fig. 8 where the hyperbolic component in axial direction is smaller, rotation "along" the orbit is only 0.3, and the orbit oscillates radially with frequency 3 and amplitude 3 and axially with frequency 4 and amplitude 0.8 per revolution.

The second model was used to generate the remaining two data sets. The data set VI, visualized in Fig. 5(c), exhibits rotation of 0.05 along the orbit and the hyperbolicity varies from maximum on one side of the orbit to zero hyperbolicity on the other side. Data set VII (Fig. 9) is the most complex one, it differs from VI in terms of slower rotation along the orbit (0.02), a 180 degree rotation around the orbit per revolution (causing a twisted-saddle periodic orbit), no variation of hyperbolicity along the orbit, but instead radial oscillation of the orbit with amplitude 2 and frequency 6, axial oscillation with amplitude 3 and frequency 5, and noise of maximum magnitude 0.005 added to the vector field. Adding higher levels of noise, however, disrupted the results of $\mathbf{v}\|\mathbf{a}$. A more sophisticated noise model could be used for this. We regard this data representative for real-world data.

Our approach obtained the periodic orbit in all cases in terms of a bifurcation line, some with refined $\mathbf{v}\|\mathbf{a}$, some with $\mathbf{v}\|\mathbf{b}$. As expected, however, it extracted only the sufficiently hyperbolic part of the orbit in data set VI. The 2D manifolds of the bifurcation line, however, obtained the complete periodic orbit due to our seed curve connection approach (Fig. 7(e)). Note that because $\mathbf{v}\|\mathbf{a}$ provided a very inaccurate result in this case, the ends of our line did not converge well to the bifurcation line during refinement.

5.2. Buoyant Flow CFD Data

Next, we applied our approach to a time-dependent simulation of buoyant air flow in a closed container, heated at the bottom and cooled at the top. This data set was simulated on a uniform grid with resolution $61 \times 31 \times 61$. Figure 1(a) shows the result obtained with traditional vector field topology while Fig. 1(b) shows the result of our approach. One can see that the 2D manifolds extracted from both approaches are consistent, although some are missing in one approach while some are missing in the other. For example, the unstable 2D manifold of the uppermost saddle point was also obtained from the bifurcation line. Nevertheless, at the same region, the stable 2D manifold could only be extracted from the bifurcation line. On the other hand,

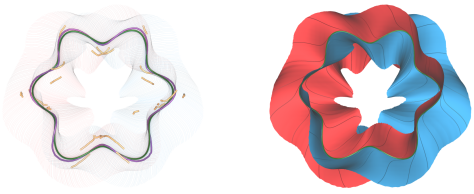

(a) (b)

Figure 9: *Twisted Saddle Orbit data set (VII). Similar to 5(a) but with orbit additionally curved in both radial and axial direction, and with noise added to the vector field. (a) Parallel vectors solutions of* $\mathbf{v}\|\mathbf{a}$ *(purple), refined* $\mathbf{v}\|\mathbf{a}$ *(green), and* $\mathbf{v}\|\mathbf{b}$ *(yellow), with some of the streamlines of the manifolds for context. The* $\mathbf{v}\|\mathbf{b}$ *criterion failed here, as in most curved periodic orbits with low tangential velocity in our experiments. (b) The manifolds of refined* $\mathbf{v}\|\mathbf{a}$.

there are cases where a critical point provides manifolds that are not related to bifurcation lines, e.g., those of spiral saddles at the bottom. This demonstrates that a merge of both approaches provides a more complete visualization of the topological structure of vector fields.

5.3. Solar MHD Data

Finally, we carried out experiments with MHD simulation data of the solar corona, available at [MHD]. These data are given on a spherical structured grid at resolution $181 \times 100 \times 150$, but since the coronal magnetic field exhibits significantly more complex structures near the solar surface, we resampled the data in regions of interest (ROI) there.

Our first investigation is in a small ROI that contains two saddle points close to each other. Figure 3(a) shows the result by means of traditional vector field topology: both critical points have been extracted and the respective 1D and 2D manifolds computed. It can be seen that both 2D manifolds converge to and are limited by the 1D manifold of the other critical point. The intersection of the two 2D manifolds represents a saddle connector. The streamlines on the 2D manifolds nicely convey that the complete saddle connector is hyperbolic, i.e., it repels streamlines in one direction along one 2D manifold while it attracts streamlines along the other 2D manifold. Figure 3(b) provides the result obtained with our approach. Because the entire saddle connector is hyperbolic, it is completely captured by the resulting bifurcation line. Note that there are also small bifurcation lines on the other side of the critical points, resulting in gaps in the 2D manifolds where the critical points reside. These gaps could be closed by connecting the bifurcation lines across the critical points prior to seed curve generation, but we omitted this in our implementation as it could introduce inaccuracies.

Another ROI captures a bifurcation line that extends from a saddle point to the domain boundary (Fig. 4). In this case, traditional vector field topology only provides one 2D manifold, see Fig. 4(a). Figure 4(b) shows the result obtained with our approach, which provided both 2D manifolds and hence

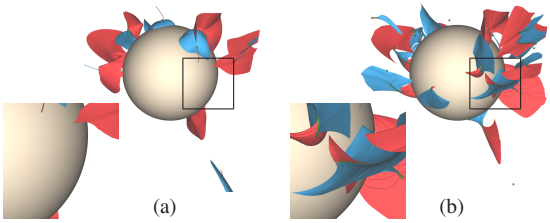

Figure 10: *Solar MHD data set. (a) Traditional visualization by means of 1D/2D manifolds (red, blue) of (spiral) saddle critical points (green). (b) Visualization based on bifurcation lines (green curves) and their 2D manifolds (red, blue). It is apparent that (a) fails to provide the field structure in regions where no critical points are present (e.g., the front of the Sun), while our visualization provides these details.*

the full topological picture. Note that the 2D manifolds are not integrated to full extent to avoid occlusion issues.

Figure 10 compares the result from traditional vector field topology with our approach. This ROI was resampled at a resolution of 201^3. As for the CFD data set, one can observe that in some regions (e.g., the highlighted one) the traditional vector field topology does not provide the full topological picture, i.e., some separating manifolds are missing, while our approach provides those and hence complements it.

6. Conclusion

We have presented local extraction of bifurcation lines by altering two existing techniques for vortex core line extraction, formulated by means of the parallel vectors operator. We have investigated the advantages and drawbacks of the two methods and, because one of them provided better results in general but failed more often, we introduced refinement of solutions of the parallel vectors operator. To obtain their 2D manifolds, similar to those of saddle points, we developed a respective seeding strategy that avoids unnecessary gaps. We related the concept of bifurcation lines to saddle connectors and saddle-type periodic orbits and found that each of these constructs has to contain at least a part of a bifurcation line. As a consequence, our technique provides a local approach to the extraction of saddle-type periodic orbits and (parts of) saddle connectors. In the case of periodic orbits, our approach works also in configurations where the velocity along the orbit is low compared to the hyperbolicity of the orbit, cases where traditional approaches based on streamline integration tend to fail. We have shown that bifurcation lines and their 2D manifolds can complete traditional vector field topology. More sophisticated refinement could be subject to future work, as well as the application of our refinement for more accurate extraction of vortex core lines and ridge lines.

Acknowledgements

This work was supported by Capes-Brazil (BEX 4097/10-6) and the German Research Foundation within the Cluster of Excellence in Simulation Technology (EXC 310/1).

References

[Asi93] ASIMOV D.: *Notes on the Topology of Vector Fields and Flows*. Tech. Rep. RNR-93-003, NASA Ames Research Center, 1993. 2

[FPH*08] FUCHS R., PEIKERT R., HAUSER H., SADLO F., MUIGG P.: Parallel vectors criteria for unsteady flow vortices. *IEEE Trans. Vis. Comput. Graphics 14*, 3 (2008), 615–626. 3

[Hal00] HALLER G.: Finding finite-time invariant manifolds in two-dimensional velocity fields. *Chaos 10*, 1 (2000), 99–108. 2

[JH95] JEONG J., HUSSAIN F.: On the identification of a vortex. *Journal of Fluid Mechanics 285*, 69 (1995), 69–94. 3

[KHL99] KENWRIGHT D. N., HENZE C., LEVIT C.: Feature extraction of separation and attachment lines. *IEEE Trans. Vis. Comput. Graphics 5*, 2 (1999), 135–144. 1

[KRRS13] KASTEN J., REININGHAUS J., REICH W., SCHEUERMANN G.: Towards the extraction of saddle periodic orbits. In *Proceedings of TopoInVis 2013* (2013). to appear. 3

[LDS90] LEVY Y., DEGANI D., SEGINER A.: Graphical visualization of vortical flows by means of helicity. *AIAA 28*, 8 (1990), 1347–1352. 3

[MHD] Predictive science modeling support for helioseismic and magnetic imager solar dynamics observatory. http://www.predsci.com/hmi/home.php. 7

[MSRT13] MARTINEZ ESTURO J., SCHULZE M., RÖSSL C., THEISEL H.: Poisson-based tools for flow visualization. In *Proceedings of IEEE PacificVis* (2013), pp. 241–248. 5

[PC87] PERRY A. E., CHONG M. S.: A description of eddying motions and flow patterns using critical-point concepts. *Annual Review of Fluid Mechanics 19* (1987), 125–155. 1, 2

[PR99] PEIKERT R., ROTH M.: The parallel vectors operator: a vector field visualization primitive. In *Proceedings of IEEE Visualization* (1999), pp. 263–270. 2, 3, 4

[PS08] PEIKERT R., SADLO F.: Height ridge computation and filtering for visualization. In *Proceedings of IEEE PacificVis* (2008), pp. 119–126. 4

[Rot00] ROTH M.: *Automatic extraction of vortex core lines and other line-type features for scientific visualization*. PhD thesis, ETH Zurich, No. 13673, 2000. 1, 3, 4

[RP98] ROTH M., PEIKERT R.: A higher-order method for finding vortex core lines. In *Proceedings of IEEE Visualization* (1998), pp. 143–150. 1, 2, 3, 4

[SH95] SUJUDI D., HAIMES R.: Identification of swirling flow in 3d vector fields. In *Proceedings of 12th AIAA Computational Fluid Dynamics Conference* (1995), pp. 95–1715. 1, 2, 3, 4

[SWH05] SAHNER J., WEINKAUF T., HEGE H.-C.: Galilean invariant extraction and iconic representation of vortex core lines. In *Proceedings of EuroVis* (2005), pp. 151–160. 3

[TWHS03] THEISEL H., WEINKAUF T., HEGE H.-C., SEIDEL H.-P.: Saddle connectors - an approach to visualizing the topological skeleton of complex 3d vector fields. In *Proceedings of IEEE Visualization* (2003), pp. 225–232. 2, 3

[WSTH07] WEINKAUF T., SAHNER J., THEISEL H., HEGE H.-C.: Cores of swirling particle motion in unsteady flows. *IEEE Trans. Vis. Comput. Graphics 13*, 6 (2007), 1759–1766. 3

[WTHS04] WEINKAUF T., THEISEL H., HEGE H.-C., SEIDEL H.-P.: Boundary switch connectors for topological visualization of complex 3D vector fields. In *Proceedings of Symposium on Visualization (VisSym '04)* (2004), pp. 183–192. 3